





## Antiferroelectricity and robust dielectric response owing to competing polar and antipolar instabilities in tetragonal tungsten bronze $K_2RNb_5O_{15}$ ( $R$ : rare-earth)

Tomoki Murata <sup>1,\*</sup>, Hirofumi Akamatsu <sup>2,†</sup>, Daisuke Hirai,<sup>1</sup> Fumiyasu Oba <sup>3</sup> and Sakyo Hirose <sup>1,‡</sup>

<sup>1</sup>*Murata Manufacturing Co., Ltd., Kyoto 617-8555, Japan*

<sup>2</sup>*Department of Applied Chemistry, Kyushu University, Fukuoka 819-0395, Japan*

<sup>3</sup>*Laboratory for Materials and Structures, Institute of Innovative Research, Tokyo Institute of Technology, Kanagawa 226-8503, Japan*



(Received 21 June 2020; accepted 1 October 2020; published 29 October 2020)

Antiferroelectricity (AFE) and its robust dielectric response under a high electric field were experimentally demonstrated in tetragonal tungsten bronze  $K_2RNb_5O_{15}$  ( $R$ : rare-earth). Electrical resistivity and density of ceramics samples were sufficiently improved by optimizing chemical compositions and processes, and the phase transition temperatures are widely controlled by changing  $R$  ions. Typical features of AFE, i.e., a double-hysteresis loop and a dielectric peak under a DC electric field, were demonstrated at room temperature in  $K_2Pr_{0.75}La_{0.25}Nb_5O_{15}$ . Notably robust relative permittivity against DC fields, which might be applicable to ceramics capacitors for high-voltage usage, is realized owing to AFE. Its dielectric constant under a high DC electric field,  $\epsilon \sim 800$  at 10 MV/m, exceeds that of conventional  $BaTiO_3$ ,  $\epsilon \sim 620$  at 10 MV/m. First-principles calculations suggested competing polar and antipolar instabilities underlying the successive phase transitions in this system. Two different types of antipolar displacement patterns ( $\Gamma_2^-$  and  $M_1^+M_4^+$ ) were found and are considered to be the structural origin of AFE. These results clearly demonstrate that  $K_2RNb_5O_{15}$  offers a new antiferroelectric materials platform that operates around room temperature.

DOI: [10.1103/PhysRevMaterials.4.104419](https://doi.org/10.1103/PhysRevMaterials.4.104419)

### I. INTRODUCTION

Applications of ferroelectric (FE) or paraelectric (PE) materials in modern electronics are governed by conventional perovskite oxides. Multilayer ceramic capacitors (MLCCs) are one of the most common electronic components and consist of well-known FE perovskite  $BaTiO_3$  [1]. Antiferroelectric (AFE) materials, where electric dipoles are aligned in an antiparallel manner and net polarization is zero [2], have been investigated over many years and have recently attracted intense interest for applications in energy storage and pulsed capacitors [3–6]. In addition, AFE materials might enable capacitors that have high capacitance under high voltage. AFE behavior is characterized by double-hysteresis polarization-field ( $P$ - $E$ ) loops [7,8] accompanied by a permittivity peak as a function of DC electric field [9]. This results in a relatively high permittivity up to high DC field, which motivates us to commercialize AFE capacitors for high-voltage usage. However, there are only limited candidate materials that host the AFE nature. The most common AFE materials are  $PbZrO_3$ -based perovskites [7,10–12], but practical applications of lead-containing materials are severely restricted. Another candidate is  $NaNbO_3$ -based perovskite [13,14] whose AFE property is not yet sufficient to attain high permittivity under the DC field. We are currently searching for a new AFE material candidate that is applicable to MLCCs for high DC

field usage such as 10 MV/m, especially in crystallographic systems other than perovskites.

Tetragonal tungsten bronze (TTB) is one of the largest families of FE or dielectric oxides next to perovskites. TTB compounds have a general formula of  $(A2)_4(A1)_2(B1)_2(B2)_8(C)_4(X)_{30}$ . As illustrated in Fig. 1(a), corner-sharing  $BO_6$  octahedra form a perovskitelike, but slightly distorted, layered network made up of pentagonal  $A2$ , quadrilateral  $A1$ , and triangular  $C$  sites. A wide range of partial occupancy is adopted at the  $A$  sites. When the  $A$  sites are fully occupied, the structure is described as “filled,” while structures with partial occupancy at the  $A$  sites are referred to as “unfilled” [15]. Partial occupancy at the  $A1$  site of less than 50% is also possible and referred to as “empty” [16,17]. The  $C$  sites are usually empty but can be occupied by small ions such as lithium, and full occupancy at the  $A$  and  $C$  sites is described as “stuffed” [18]. A wide variety of cations and partial occupancy at the  $A$  sites enables abundant compositional diversity and a substantial possibility for property manipulation in the TTB system [19].

The aristotype of the TTB structure has a space group of  $P4/mbm$  and approximate lattice constants of  $a_t \sim 12.5$  Å and  $c_t \sim 4$  Å. The simplest FE structure is noncentrosymmetric  $P4bm$  with the same cell dimensions. For some TTBs, there is an orthorhombic distortion owing to octahedral tilts, which requires a  $45^\circ$  rotation and  $\sqrt{2}$  expansion of the unit cell in the  $ab$  plane with cell doubling along the  $c$  axis (such that  $a' = \sqrt{2}a_t$  and  $c' = 2c_t$ ) and has a space group of  $Ima2$  [20]. Further unit cell doublings in the  $ab$  plane [21] or incommensurate modulations [22] have also been reported. The polarization in TTB is usually  $c$ -axis oriented and originates

\*Corresponding author: tomoki.murata258@murata.com

†h.akamatsu@cstf.kyushu-u.ac.jp

‡h\_sakyo@murata.com

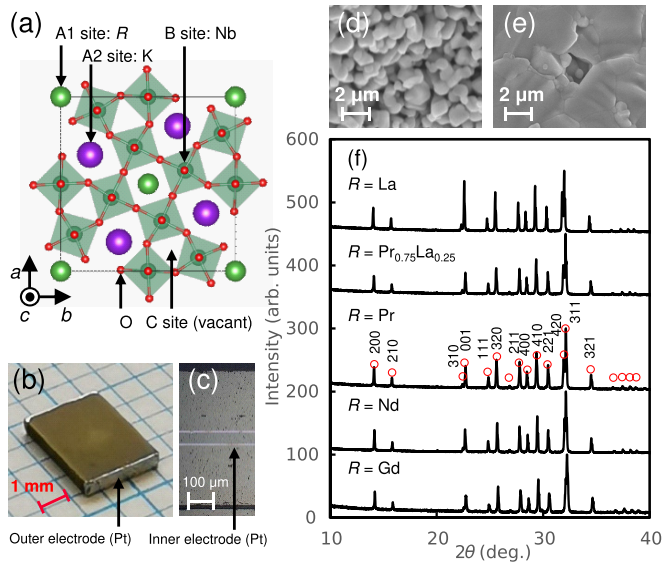


FIG. 1. (a) Crystal structure of TTB  $K_2RNb_5O_{15}$ . (b) MLCC sample of  $K_2PrNb_5O_{15}$ . (c) Cross-sectional image of MLCC sample taken with an optical microscope. (d), (e) SEM images of fracture surfaces of sintered  $K_2PrNb_5O_{15}$  ceramics (d) without Mn and (e) with Mn. (f) XRD patterns of sintered ceramics with the compositions  $R = La, Pr_{0.75}La_{0.25}, Pr, Nd, Gd$ . Red circles indicate peak positions and relative intensities of a simulated profile for  $R = Pr$  based on the aristotype  $P4/mbm$  cell. Indexing is also based on the  $P4/mbm$  cell.

from  $B$ -site ion displacements in the  $BO_6$  octahedra, whereas  $Pb^{2+}$  [23] or  $Bi^{3+}$  [24] at the  $A$  site stabilizes polar displacements within the  $ab$  plane. As the structural distortions described above are quite small, it is usually difficult to detect them using laboratory x-ray diffraction. It requires selected area electron diffractions or high-resolution diffraction using synchrotron x-ray or neutron beams to distinguish between these distorted structures.

Here, we focus on a filled TTB system of  $K_2RNb_2O_5$  ( $R$ : rare-earth) [Fig. 1(a)] as a candidate AFE at room temperature ( $\sim 300$  K).  $K_2RNb_2O_5$  has been reported to have two dielectric anomalies against temperature [25,26], which are assumed to be FE-AFE and AFE-PE transitions [27]. These anomalies are consistent with the peaks observed in calorimetry measurement. There is a clear first-order phase transition with a large amount of thermal hysteresis and heat absorption (or emission) between the assumed FE and AFE phases [27], and two successive phase transitions of this kind are relatively rare among TTB compounds. However, evidence of AFE properties, such as a double-hysteresis loop and robust dielectric response to an electric field, as well as detailed structural data containing atomic coordinates, has not yet been reported. It is still unclear whether the assumed FE and AFE phases have the appropriate dielectric properties to qualify as FE and AFE. In this study, we have attempted to fabricate highly insulated  $K_2RNb_2O_5$  MLCCs and measured their dielectric responses under electric fields and demonstrated room temperature AFE properties by tailoring chemical compositions in  $K_2RNb_2O_5$ . First-principles calculations were also performed on  $K_2RNb_2O_5$  to examine polar and antipolar

structural instabilities underlying the mechanisms of phase transitions in this system.

## II. EXPERIMENTAL AND COMPUTATIONAL DETAILS

MLCCs of  $K_2RNb_5O_{15}$  ( $R = La, Pr, Nd, Gd$ ) with Pt-inner electrodes as shown in Fig. 1(b), where the effective electrode area and dielectric thickness of the dielectric layer are  $\sim 3$  mm<sup>2</sup> and 48  $\mu m$ , respectively, were prepared by conventional solid state reactions and the existing MLCC processes. The starting materials,  $K_2CO_3, La_2O_3, Pr_6O_{11}, Nd(OH)_3, Gd_2O_3,$  and  $Nb_2O_5$ , were dried before being weighed and ball-milled in ethanol with partially stabilized zirconia balls for 16 h. After calcination at 1473 K for 20 h, the obtained  $K_2RNb_5O_{15}$  powders were mixed with 2.5 mol %  $MnCO_3$  and ball-milled in organic solvent with binder for 20 h. Green sheets were fabricated using a tape-casting method with a doctor blade with a 200- $\mu m$  gap. The inner electrode was printed with Pt paste using a screen-printing method. The green sheets were laminated, pressed, and cut to obtain green chips. The chips were heated up to 773 K to burn out the binders and sintered at 1573–1598 K for 2 h. To suppress the evaporation of potassium ions while sintering, the chips were placed into a dense alumina crucible with the calcined powder of the same composition. The cross-sectional image of the sintered MLCC samples shown in Fig. 1(c) shows a smooth and straight interface between the Pt-inner electrodes and ceramics without any noticeable defects or delamination, indicating that our samples were nicely fabricated as intended. Plate samples without inner Pt electrodes were also fabricated and pulverized for structural analysis using x-ray diffraction (XRD; Rigaku SmartLab 3). A scanning electron microscope (SEM) was employed to observe fracture surfaces. Electric polarization and relative permittivity were measured under electric fields up to 1 kV using a ferroelectric tester (Radiant Premier II) and LCR meter (Agilent E4980A) with an external voltage source (Keithley 6517B), respectively.

First-principles calculations were conducted to predict polar and antipolar structural instability in  $K_2RNb_5O_{15}$  for  $R = La, Nd, Sm, Gd,$  and  $Dy$ . The projector augmented-wave method [28,29] was used with the PBEsol functional [30–32] as implemented in the Vienna *Ab initio* Simulation Package (VASP) code [33–36]. Standard projector augmented-wave datasets were employed with a plane-wave cutoff energy of 550 eV. The following states were treated as valence electrons:  $3p$  and  $4s$  for K;  $5s, 5p, 5d,$  and  $6s$  for La, Nd, and Sm;  $5p, 5d,$  and  $6s$  for Gd and Dy;  $4p, 4d,$  and  $5s$  for Nb; and  $2s$  and  $2p$  for O. The lattice constants and internal coordinates were optimized until the residual stress and force were converged to 0.04 GPa and 10 meV/ $\text{\AA}$ , respectively. The phonon band dispersion curves of  $K_2LaNb_5O_{15}$  with the aristotype  $P4/mbm$  structure were derived using the PHONOPY code [37] from the force constants calculated for its  $2 \times 2 \times 2$  supercells. A  $1 \times 1 \times 2$   $k$  mesh in the Monkhorst-Pack scheme was used [38], granting sufficient  $k$ -mesh density due to the large metrics of the supercell ( $\sim 25 \times 25 \times 8$   $\text{\AA}^3$ ). A phonon band path connecting high-symmetry  $k$  points was generated using the SUMO code [39]. The stable structure search was conducted to search for atomic displacement patterns that lower symmetry

and total energy. Atomic displacements in accordance with each unstable phonon mode were added to the aristotype  $P4/mbm$  structure, followed by a full structural relaxation under symmetry constraints. Space group symmetry of the relaxed structure was determined using the SPGLIB code [40]. When the relaxed structure has a different space group and lower total energy than the  $P4/mbm$  phase, the structure is considered to be a candidate for a low-temperature polar or antipolar phase. As a frequently reported FE structure of TTB has a  $\sqrt{2} \times \sqrt{2} \times 2$  unit cell expansion due to octahedral tiltings (typically with space group  $Ima2$ ), we expect that  $\sqrt{2} \times \sqrt{2} \times 2$  expansion is sufficient to represent polar or antipolar structures in  $K_2RNb_5O_{15}$ . Therefore, we tracked instabilities for the  $\sqrt{2} \times \sqrt{2} \times 2$  supercell of the  $P4/mbm$  structure at the  $\Gamma$  point, into which the  $M$ -,  $A$ -, and  $Z$ -point phonon modes are folded. A  $2 \times 2 \times 2$  Monkhorst-Pack  $k$  mesh was used for the supercells with cell metrics of  $\sim 18 \times 18 \times 8 \text{ \AA}^3$  and 184 atoms. Structural distortions were decomposed into symmetry-adapted modes using ISODIS-TORT from the ISOTROPY software suite [41]. In order to predict electric polarization, Born effective charge tensor components were obtained by using the density functional perturbation theory (DFPT) calculation implemented in the VASP code. A larger plane-wave cutoff energy (700 eV) and a finer  $k$  mesh ( $4 \times 4 \times 4$ ) for the  $\sqrt{2} \times \sqrt{2} \times 2$  supercell of the  $P4/mbm$  structure were employed for the DFPT calculations. Crystal orbital Hamiltonian population (COHP) was computed using the LOBSTER code [42–45] in order to estimate stabilization energies for covalent bond formation. Bond valence sum (BVS) was calculated for the optimized structures using the bond valence parameters [46] with the aid of the pymatgen python library [47]. We utilized the VESTA code to visualize the crystal structure [48].

### III. RESULTS AND DISCUSSION

#### A. Microstructure and crystal structure of $K_2RNb_5O_{15}$ -MLCC samples

The dielectric properties under a high electric field in  $K_2RNb_5O_{15}$  have not been reported yet, as the electrical resistivity of the ceramics samples in previous reports does not seem to be adequately high [24–27]. Here we have successfully improved the resistivity of  $K_2RNb_5O_{15}$  ceramics by adding manganese (Mn) oxide as a sintering aid and modifying sintering atmosphere as described in the methods section. Figures 1(d) and 1(e) show the fracture surfaces of  $K_2PrNb_5O_{15}$  MLCCs without and with Mn, respectively. The ceramics without Mn have substantial porosity, as previously reported [24], and show poor resistivity. By adding Mn, dense ceramics, where the porosity is significantly reduced and the grain size is increased to  $\sim 2 \mu\text{m}$ , were obtained. MLCCs made from  $K_2RNb_5O_{15}$  with Mn show sufficient electrical insulation yielding low dielectric loss  $\tan\delta$ , as discussed later, which enables us to apply high electric fields to  $K_2RNb_5O_{15}$  MLCCs.

We selected  $R = \text{La, Pr, Nd, and Gd}$  as rare-earth ions and synthesized their solid solutions to investigate the dependence of dielectric properties on the ionic radius of  $R$  at the  $A1$

TABLE I. Compositions of rare-earth ions  $R$  in  $K_2RNb_5O_{15}$  and average ionic radii of  $R$  for the ninefold coordination [51] of the fabricated samples.

Composition of $R$	Average ionic radii of $R$ ( $\text{\AA}$ )
La	1.216
$\text{Pr}_{0.5}\text{La}_{0.5}$	1.198
$\text{Pr}_{0.75}\text{La}_{0.25}$	1.188
$\text{Pr}_{0.85}\text{La}_{0.15}$	1.185
Pr	1.179
$\text{Pr}_{0.25}\text{Nd}_{0.75}$	1.175
$\text{Pr}_{0.5}\text{Nd}_{0.5}$	1.171
$\text{Pr}_{0.25}\text{Nd}_{0.75}$	1.167
Nd	1.163
$\text{Pr}_{0.5}\text{Gd}_{0.5}$	1.143
$\text{Pr}_{0.25}\text{Gd}_{0.75}$	1.125
Gd	1.107

sites. Among the selected rare-earth ions, La is the largest, followed by Pr, Nd, and Gd. The investigated compositions and their (average)  $R$  ionic radii are summarized in Table I. Figure 1(f) shows the XRD profiles of the representative sintered ceramics. Phase-pure TTB ceramics were obtained for all compositions including solid solutions. Red circles and indices in Fig. 1(f) denote simulated peak positions and relative intensities for  $K_2PrNb_5O_{15}$  based on the aristotype cell of the TTB structure (space group  $P4/mbm$ ). As described above, TTB structures can adopt several different symmetries, which are relevant to different distortions such as polar displacements and  $\text{NbO}_6$  octahedral tilts, yielding space groups such as  $P4bm$  and  $Ima2$ . These distortions are usually so subtle that it is difficult to distinguish between them using laboratory XRD. Therefore, in this study, we simply checked the phase purity and estimate pseudotetragonal lattice constants  $a_t$  and  $c_t$  of each composition based on the aristotype  $P4/mbm$  structure. The lattice constants and  $c_t/a_t$  ratio are calculated from the 420 and 311 peaks and plotted as a function of the rare-earth radius in Figs. 4(b)–4(d), as detailed later.

#### B. Ferroelectric and antiferroelectric properties of $K_2RNb_5O_{15}$

The relative permittivity and dielectric loss  $\tan\delta$  as a function of temperature are shown in Fig. 2 for representative compositions. All the ceramics samples show sufficient electrical insulation yielding low values of  $\tan\delta$  up to  $\sim 500$  K. An upturn of  $\tan\delta$  above 500 K in the composition  $R = \text{Gd}$  indicates an emergence of a leakage current contribution. To clarify dielectric anomalies at high temperatures with excluding the leakage, data measured at a higher frequency (100 kHz) is shown for the composition  $R = \text{Gd}$  in Fig. 2(a), while data measured at 1 kHz is shown for the compositions  $R = \text{Nd, Pr, and Pr}_{0.75}\text{La}_{0.25}$  in Figs. 2(b)–2(d). The compositions  $R = \text{Gd, Nd, Pr, and Pr}_{0.75}\text{La}_{0.25}$  show two anomalies in relative permittivity, which can be attributed to two phase transitions from FE to AFE to PE, according to the previous report [27]. The lower transition temperature associated with a FE-AFE transition is defined as  $T_{C1}$  and the higher one with an AFE-PE transition is defined as  $T_{C2}$ .  $T_{C1}$  has a large amount of thermal hysteresis (typically 10–45 K), so

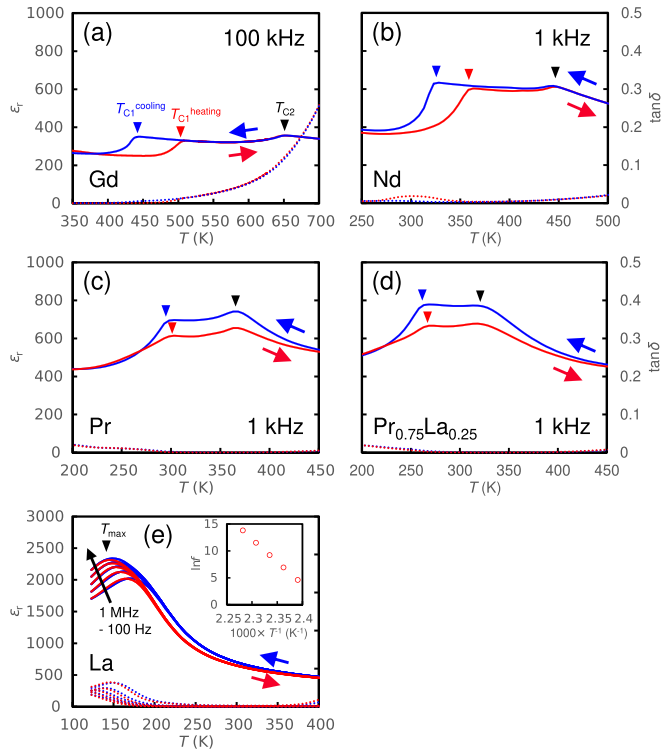


FIG. 2. Relative permittivity (left axis, solid curve) and dielectric loss  $\tan\delta$  (right axis, dotted curve) as a function of temperature for the representative compositions. Data measured at selected frequency is shown for (a)  $R = \text{Gd}$ , (b)  $R = \text{Nd}$ , (c)  $R = \text{Pr}$ , and (d)  $R = \text{Pr}_{0.75}\text{La}_{0.25}$ . Red and blue curves denote heating and cooling processes, respectively. Colored triangles indicate phase transition temperatures  $T_{C1}^{\text{heating}}$ ,  $T_{C1}^{\text{cooling}}$ , and  $T_{C2}$ . Data measured in a frequency range of 100 Hz–1 MHz (100 Hz, 1 kHz, 10 kHz, 100 kHz, 1 MHz) are shown for (e)  $R = \text{La}$ . The inset in (e) shows logarithmic measurement frequency against the inverse of dielectric peak temperature. Triangle indicates peak temperature of data measured at 100 Hz.

$T_{C1}^{\text{heating}}$  and  $T_{C1}^{\text{cooling}}$  are also defined, while  $T_{C2}$  shows a relatively small amount of thermal hysteresis ( $<3$  K). The phase transition temperatures for the composition  $R = \text{Gd}$  are  $T_{C1}^{\text{heating}} = 503$  K,  $T_{C1}^{\text{cooling}} = 445$  K, and  $T_{C2} = 655$  K, which nearly correspond with those of the previous report [27]. With increasing the (average) ionic radius of  $R$  from Gd [Fig. 2(a)] to La [Fig. 2(e)],  $T_{C1}$ ,  $T_{C2}$ , and the amount of thermal hysteresis decreases, and the relative permittivity increases. Note that the composition  $R = \text{Pr}_{0.75}\text{La}_{0.25}$  has a  $T_{C1}$  of approximately  $\sim 273$  K ( $\sim 0^\circ\text{C}$ ) and a  $T_{C2}$  of 328 K ( $55^\circ\text{C}$ ), granting the AFE phase at room temperature, which will be demonstrated later. The temperature range of the AFE phase is successfully modified by tuning the ionic radius of  $R$ . On the other hand, the composition  $R = \text{La}$  shows a single anomaly with a large frequency dispersion, which is considered to be a relaxor behavior [Fig. 2(e)]. Among the compositions investigated in the present study, the relaxor nature is observed only with large (average) ionic radii of  $R = \text{La}$  and  $\text{La}_{0.5}\text{Pr}_{0.5}$  (data not shown for the latter).

To elucidate the dielectric properties of each temperature phase, a dielectric response under a high electric field

was investigated on the composition  $R = \text{Pr}_{0.75}\text{La}_{0.25}$  and  $R = \text{La}$ .  $P$ - $E$  data along with current-field ( $I$ - $E$ ) data are shown in Fig. 3. The current  $I$  is formulated as  $I = dP/dE$  and increases when a drastic change in net polarization, i.e., polarization reversal or phase transition, occurs. In the low-temperature phase of  $R = \text{Pr}_{0.75}\text{La}_{0.25}$  at 223 K, a well-saturated FE  $P$ - $E$  loop is observed. The peaks in the  $I$ - $E$  data seen when loading the field correspond to the polarization reversal. In the intermediate temperature phase at 283 K, the  $P$ - $E$  loop has a pinched shape with zero net residual polarization, which is known as a double-hysteresis loop and typical for AFE. The characteristics associated with this pinched behavior also appear in the  $I$ - $E$  data [49]. The peaks while loading and unloading the field correspond to the phase changes between nonpolar (antipolar) and polar phases. A “backswitching” event denoted by the red triangles in Fig. 3(b) is an important feature of AFE, indicating that the polar phase with a finite net polarization switches back to the nonpolar (antipolar) phase with zero net polarization when unloading the field. The electric field against which the polarization backswitches is defined as backswitching field  $E_b$ . The value of  $E_b$  is 5.4 MV/m at 283 K. In the high-temperature phase at 353 K, the loop is almost linear and PE-like, though there remains a minor signature of the switching and back-switching events. In contrast, the composition  $R = \text{La}$  does not show any sign of AFE behavior. Below the dielectric peak temperature, there is a slim hysteresis loop with a small amount of residual polarization, as shown in Fig. 3(d) for 133 K. Above the dielectric peak temperature, as in the case of 203 K, there is a slim nonlinear loop without any residual polarization, while the polarization gradually saturates under an electric field [Fig. 3(e)]. These features are typical for relaxors [50], and there is no AFE signature.

### C. Phase diagram of $\text{K}_2\text{RnB}_5\text{O}_{15}$ system

Figure 4(a) shows the dielectric phase transition temperatures as a function of the (average) ionic radius of the rare-earth ions  $R$ . The ionic radii for the ninefold coordination [51] are used because there is no data available for some rare-earth ions in the actual 12-fold coordination of the A1 sites.  $T_{C1}^{\text{heating}}$ ,  $T_{C1}^{\text{cooling}}$ , and  $T_{C2}$ , which are determined from the dielectric peaks, are plotted for the composition  $R = \text{Pr}_{0.75}\text{La}_{0.25}$  and those with smaller  $R$  ionic radii. The dielectric peak temperature  $T_{\text{max}}$  at 100 Hz is also indicated for  $R = \text{Pr}_{0.5}\text{La}_{0.5}$  and La. As explained above,  $T_{C1}^{\text{heating}}$ ,  $T_{C1}^{\text{cooling}}$ , and  $T_{C2}$  decrease and finally merge into a single relaxor peak with increasing the (average) ionic radius of  $R$ , while with smaller ionic radii there emerges the intermediate temperature AFE phase. A similar trend is observed in different TTB systems such as  $\text{Ba}_4\text{R}_{0.67}\text{Nb}_{10}\text{O}_{30}$  [16],  $\text{Ba}_4\text{R}_2\text{Nb}_6\text{Ti}_4\text{O}_{30}$  [52], and  $\text{Sr}_5\text{RnB}_7\text{Ti}_3\text{O}_{30}$  [53], in which the ferroelectric Curie temperature decreases and relaxor behavior emerges as the ionic radius of  $R$  increases. The tendency observed here in  $\text{K}_2\text{RnB}_5\text{O}_{15}$  could be analogously understood with them, whereas the emergence of the AFE phase is a unique feature to  $\text{K}_2\text{RnB}_5\text{O}_{15}$ .

The variation in pseudotetragonal lattice constants,  $a_t$  and  $c_t$ , shown in Figs. 4(b) and 4(c), respectively, is also attributed to the FE-AFE-PE phase transitions. As the lattice constants

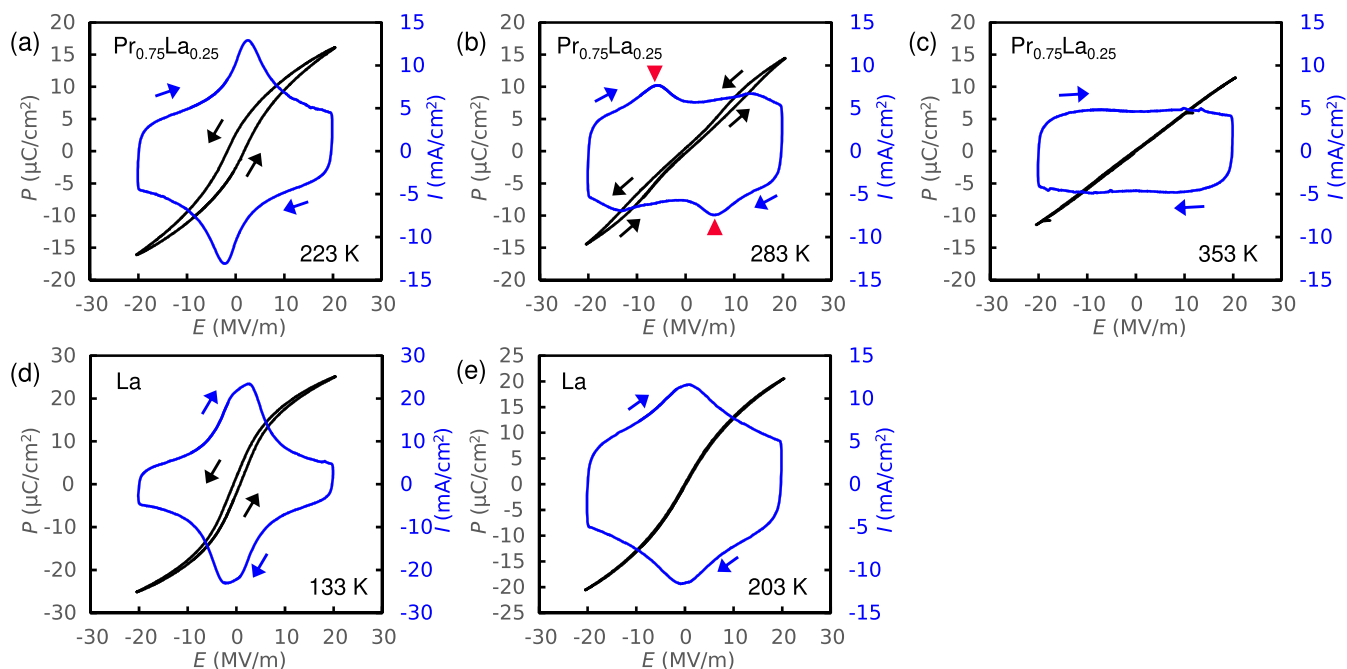


FIG. 3. (a)–(e) Polarization-field ( $P$ - $E$ ) loops along with current-field ( $I$ - $E$ ) loops for the composition  $R = \text{Pr}_{0.75}\text{La}_{0.25}$  at (a) 223, (b) 283, and (c) 353 K and for the composition  $R = \text{La}$  at (d) 113 and (e) 203 K. Black and blue curves denote  $P$ - $E$  and  $I$ - $E$  curves, respectively, and arrows indicate the sweep direction of electric field. All data were collected at 40 Hz.

are measured at ambient temperature, their variation reflects the phase change at room temperature ( $\sim 300$  K). The tetragonality  $c_t/a_t$ , indicating a degree of tetragonal distortion, is also plotted in Fig. 4(d). The broken lines in Figs. 4(b)–4(d) separate the dielectric phases at room temperature. The lattice constant  $a_t$  value increases when the (average) ionic radius of  $R$  increases and fits Vegard's law well, while the  $c_t$  value does not obey the law over the whole composition range. There is a stepwise change in the  $c_t$  value at the FE-AFE phase boundary and a kink at the AFE-PE boundary. The tetragonality,  $c_t/a_t$ , also shows a stepwise decrease at the phase change from FE to AFE. The trend in lattice constants against the phase changes is identical with the temperature variation of lattice constants reported for the composition  $R = \text{Gd}$  [27] and thus assumed to reflect the crystallographic nature of each phase.

AFE behavior in nonperovskite materials is rare, and to the best of our knowledge, indisputable AFE properties in TTB have not yet been reported, though pinched AFE-like  $P$ - $E$  loops have been reported in several TTBs.  $\text{Ba}_4\text{R}_{0.67}\text{Nb}_{10}\text{O}_{30}$  shows pinched hysteresis loops between two dielectric anomalies at 260 and 480 K, whereas well-saturated FE loops are observed below 260 K [49]. There is no change in crystallographic symmetry across 260 K, and the structure is identified as noncentrosymmetric  $Ama2$  with an expanded unit cell metric of  $2\sqrt{2}a_t \times \sqrt{2}a_t \times 2c_t$  up to 480 K. This pinched behavior is attributed not to FE-AFE but to order-disorder phase transitions, in which local polarization is disordered at some length scale and aligned by an external electric field.  $\text{Ba}_4\text{R}_2\text{Ti}_4\text{Nb}_6\text{O}_{30}$  also shows a pinched hysteresis loop, but the proposed mechanism is slightly different [54]. A typical FE hysteresis loop is observed at 293 K and a pinched loop at 473 K, whereas there is no dielectric anomaly between 293 and 473 K. This pinched

behavior is described as the incommensurate-commensurate phase change, in which an incommensurate phase with no net polarization switches to a FE commensurate phase only when an external field is applied. There are two different TTB systems hosting pinched  $P$ - $E$  loops, however, neither of which is attributed to AFE. The FE and AFE properties associated with a clear first-order phase transition, which are demonstrated by our results, are a unique and distinctive feature to  $\text{K}_2\text{RNb}_5\text{O}_{15}$  among TTB compounds.

#### D. Relative permittivity under DC electric field

It is important to validate the AFE response under a DC electric field. Relative permittivity and dielectric loss  $\tan\delta$  in the composition  $R = \text{Pr}_{0.75}\text{La}_{0.25}$  are measured up to  $\sim 15$  MV/m and in a temperature range of 223–423 K (Fig. 5). As shown in the inset of Fig. 5(b), in the FE phase at 223 K, the relative permittivity simply decreases as the DC field increases. In the AFE phase at 283 K ( $10^\circ\text{C}$ ) and 298 K ( $25^\circ\text{C}$ ), the relative permittivity initially increases, has a peak, and then decreases as the DC field increases. The peak electric field is 7.2 MV/m at 283 K and almost correspondent with  $E_b = 5.4$  MV/m derived from the  $P$ - $E$  loop. A similar dielectric peak under an electric field is observed in  $(\text{Pb}, \text{La})(\text{Zr}, \text{Sn}, \text{Ti})\text{O}_3$  [9] and this is one of the distinctive features of AFE. Figure 5(a) shows the temperature dependencies of relative permittivity under different DC field values. With DC fields of 9.4 MV/m or higher, there is only one anomaly, while with 3.1 MV/m or lower there are two anomalies corresponding to the FE-AFE-PE transitions. As the DC fields increase,  $T_{C1}$  increases and  $T_{C2}$  decreases, and finally,  $T_{C1}$  and  $T_{C2}$  merge into a single anomaly. The temperature range of the AFE phase gradually becomes narrower and van-

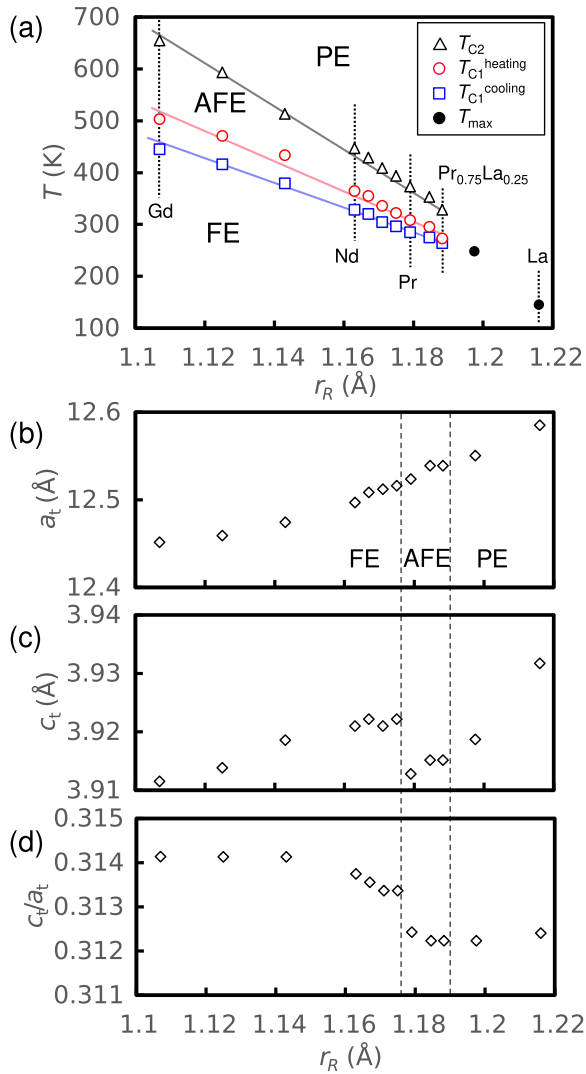


FIG. 4. (a) Phase transition temperatures as a function of the (average) ionic radius of the rare-earth ions.  $T_{C1}^{\text{heating}}$ ,  $T_{C1}^{\text{cooling}}$ , and  $T_{C2}$  determined from dielectric peaks are shown for the composition  $R = \text{Pr}_{0.75}\text{La}_{0.25}$  and those with smaller ionic radii. The dielectric peak temperature  $T_{\text{max}}$  at 100 Hz is shown for  $R = \text{Pr}_{0.5}\text{La}_{0.5}$  and La. (b)–(d) Pseudotetragonal lattice constants (b)  $a_t$  and (c)  $c_t$  and (d) tetragonality  $c_t/a_t$  against the (average) ionic radius. Horizontal axis has the same scale as (a). Dashed lines indicate dielectric phase boundaries at room temperature.

ishes under high DC fields, and the single anomaly observed in a high DC field is considered to correspond to a direct phase transition from FE to PE. This is also consistent with a conventional  $E$ - $T$  phase diagram of AFE [55].

Figure 5(b) compares relative permittivities under DC fields for  $\text{K}_2\text{Pr}_{0.75}\text{La}_{0.25}\text{Nb}_5\text{O}_{15}$  and a conventional  $\text{BaTiO}_3$ -based MLCC fabricated by almost the same method as described above. The relative permittivity of  $\text{BaTiO}_3$  sharply decreases as the DC field increases because of the saturation of the FE polarization under high electric field, while  $\text{K}_2\text{Pr}_{0.75}\text{La}_{0.25}\text{Nb}_5\text{O}_{15}$  shows a quite stable relative permittivity up to 15 MV/m owing to AFE. The relative permittivity under a high DC electric field of  $\text{K}_2\text{Pr}_{0.75}\text{La}_{0.25}\text{Nb}_5\text{O}_{15}$ ,  $\sim 800$  at 10 MV/m, exceeds that

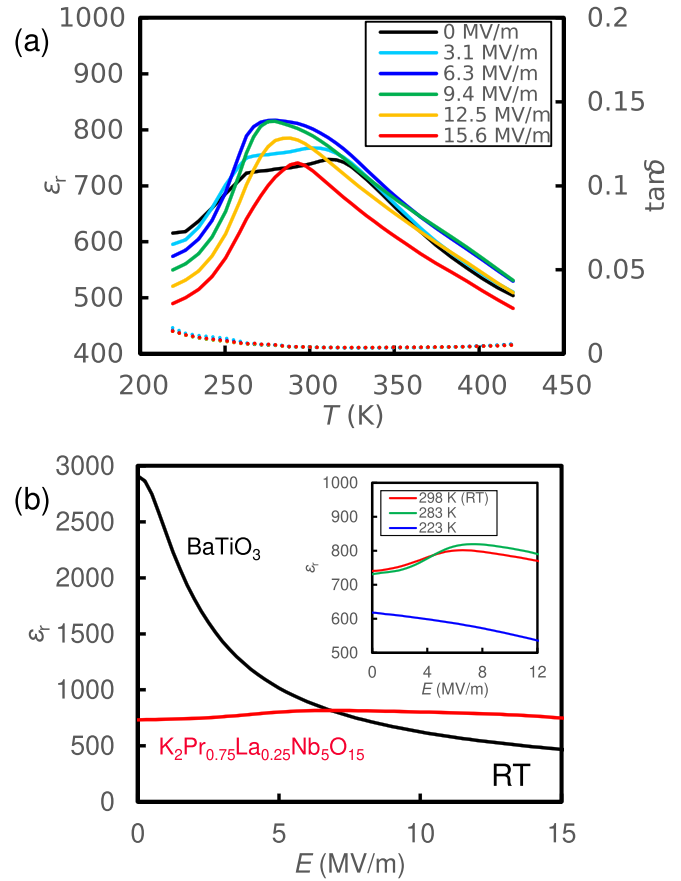


FIG. 5. (a) Relative permittivity (left axis, solid curves) and dielectric loss  $\tan\delta$  (right axis, dashed curves) of  $\text{K}_2\text{Pr}_{0.75}\text{La}_{0.25}\text{Nb}_5\text{O}_{15}$  under different DC electric fields. (b) Comparison of relative permittivity as a function of DC electric field at room temperature (RT) of 298 K (25 °C) between  $\text{K}_2\text{Pr}_{0.75}\text{La}_{0.25}\text{Nb}_5\text{O}_{15}$  and conventional  $\text{BaTiO}_3$ . Inset shows relative permittivity of  $\text{K}_2\text{Pr}_{0.75}\text{La}_{0.25}\text{Nb}_5\text{O}_{15}$  at 223, 283, and 298 K. Measurement frequency is 1 kHz.

of  $\text{BaTiO}_3$ ,  $\sim 620$  at 10 MV/m. This robust dielectric response under the DC field might be useful for designing a next-generation MLCC with stable capacitance under high voltage, though the physical origins of AFE, i.e., the structural origins of AFE in the TTB structure, are still unclear. Therefore, we conducted first-principles calculations to investigate structural origins of the AFE nature in TTBs.

### E. Theoretical investigation into polar and antipolar instabilities

The first-principles calculations were performed for  $\text{K}_2\text{LaNb}_5\text{O}_{15}$  as detailed in the methods section. First-principles studies of TTB compounds have been reported [56–58], but not with the motivation of searching for more stable, distorted structures with large unit cells. Calculated lattice constants of  $\text{K}_2\text{LaNb}_5\text{O}_{15}$  with the aristotype  $P4/mbm$  structure,  $a_t = 12.689$  Å and  $c_t = 3.945$  Å, well reproduce the experimental lattice constants. Figure 6(a) presents a phonon band structure for the  $P4/mbm$  phase in the first Brillouin zone. The dispersion curves indicate a large number of unstable phonon bands. In particular, one can see strong structural instabilities along the  $\Gamma$ - $X$ - $M$ - $\Gamma$  line, as reflected by very flat

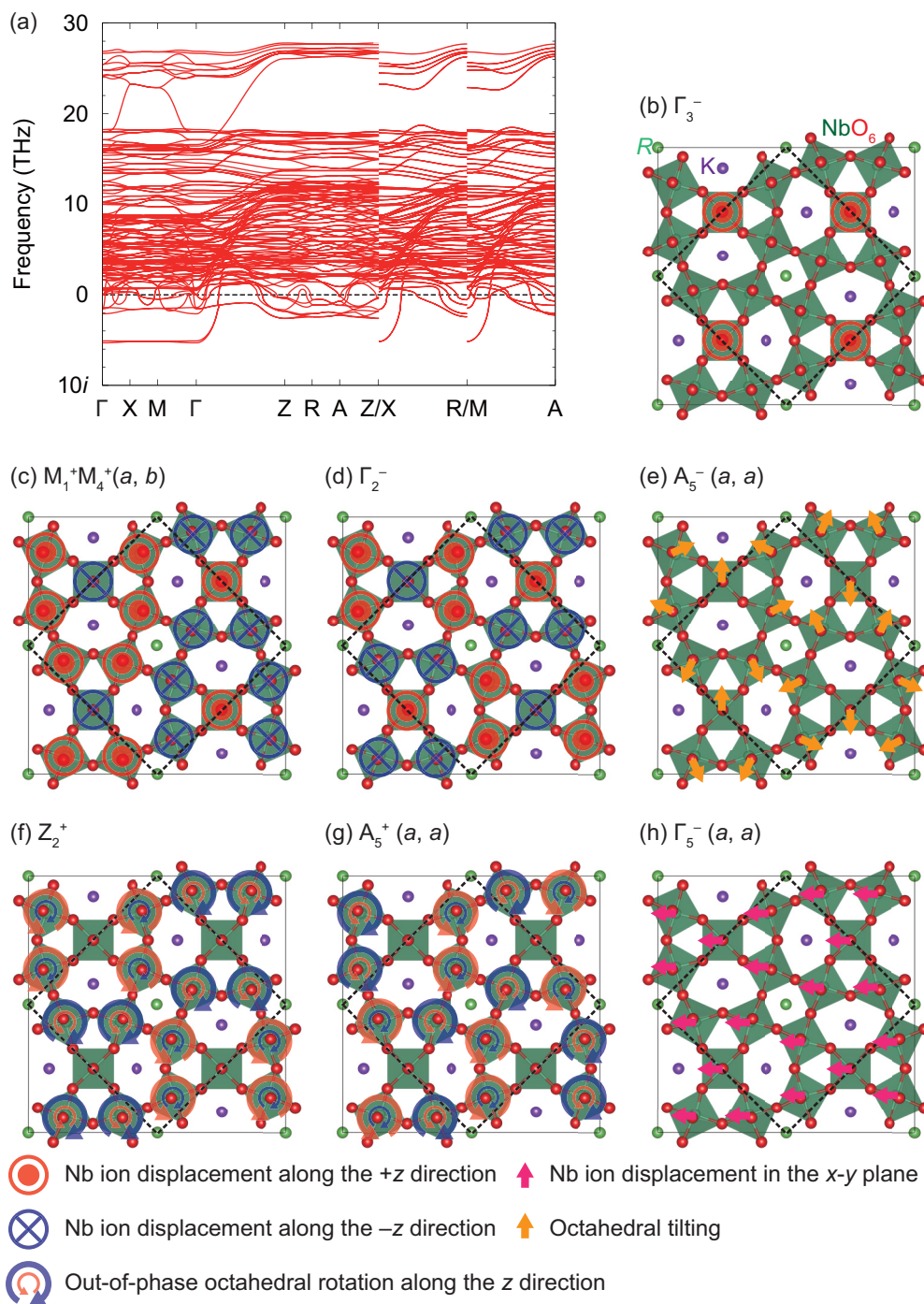


FIG. 6. (a) Calculated phonon band structure for  $K_2LaNb_5O_{15}$  with the  $P4/mbm$  structure. (b)–(h) Schematic illustrations of representative atomic displacement patterns transforming like irreps (b)  $\Gamma_3^-$ , (c)  $M_1^+M_4^+(a, b)$ , (d)  $\Gamma_2^-$ , (e)  $A_5^-(a, a)$ , (f)  $Z_2^+$ , (g)  $A_5^+(a, a)$ , and (h)  $\Gamma_5^-(a, a)$ . Displacement patterns are overlaid on the reference  $P4/mbm$  structure viewed from the  $[001]$  direction. Dashed lines indicate the unit cell.

bands at a frequency of  $\sim 5.5i$  THz. Figures 6(b)–6(d) depict schematic illustrations of the atomic displacements associated with the unstable phonon modes at the  $\Gamma$  and  $M$  points. The polar  $\Gamma_3^-$  mode with an isotropy subgroup of  $P4bm$  [Fig. 6(b)] involves off-centering motions of the Nb ions at the  $B1$  sites in the same direction, i.e.,  $+z$  or  $-z$ . Figures 6(c) and 6(d) illustrate the antipolar  $M_1^+M_4^+(a, b)$  and  $\Gamma_2^-$  modes (isotropy subgroups:  $Pmnm$  and  $P\bar{4}2_1m$ ), respectively, in which the direction of the off-centering motions of half of the Nb ions is

opposite to that of the other half. The  $M_1^+M_4^+(a, b)$  distortion is accompanied by a  $\sqrt{2} \times \sqrt{2} \times 1$  expansion of the unit cell. Thus, the coexistence of polar and antipolar instabilities is revealed for  $K_2LaNb_5O_{15}$ . The unstable modes at the  $X$  point with a frequency of approximately 5.5i THz involve an antipolar displacement pattern similar to those of the  $\Gamma_2^-$  and  $M_1^+M_4^+(a, b)$  modes. However, the cell expansion due to the condensation of the phonon modes at the  $X$  point  $(0,1/2,0)$  is beyond the scope of the present study.

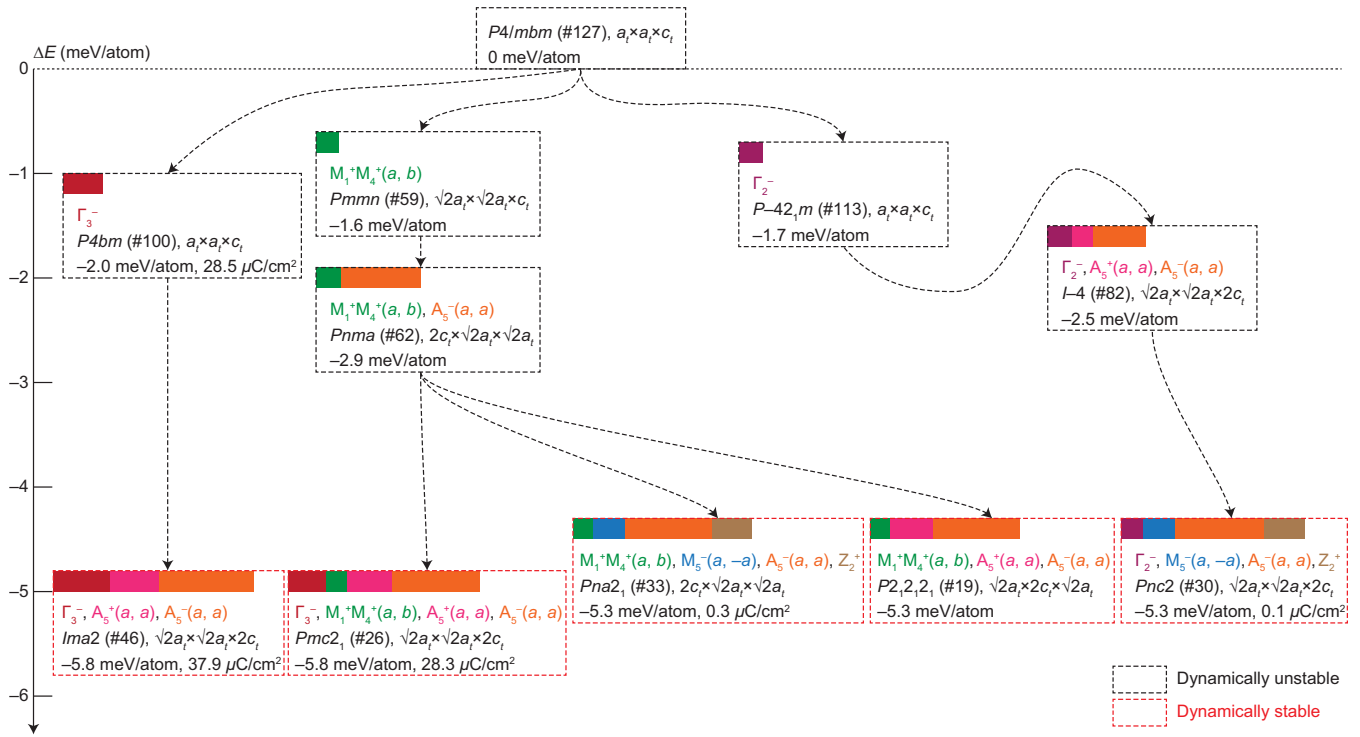


FIG. 7. The most relevant phases discovered through the stable structure search based on phonon calculations for  $\text{K}_2\text{LaNb}_5\text{O}_{15}$ . Vertical axis indicates total energies relative to that of the aristotype  $P4/mbm$  structure. Space groups, unit cell metrics, and total energies are given as well as polarization for polar phases. The arrows between the phases mean that the phase connected to the tail of the arrow shows phonon instability leading to the phase connected to the head of the arrow. The amplitude of main symmetry-adapted modes included in the total atomic displacements with respect to the  $P4/mbm$  structure is represented by the width of colored bars for each phase. The black and red dashed rectangles indicate dynamically unstable and stable phases, respectively.

Freezing of the unstable phonon modes in the aristotype  $P4/mbm$  phase, followed by full structural optimizations under symmetry constraints and the subsequent phonon calculations, enabled us to search for lower-symmetry and lower-energy structures including metastable and ground-state phases. Figure 7 summarizes the space groups and total energies of the most relevant distorted phases as well as the irreducible representations (irreps) of their main distortion modes with regard to the reference  $P4/mbm$  structure, electric polarization, and unit cell metrics, utilizing a comprehensible representation adopted in Ref. [59]. The vertical axis indicates total energies  $\Delta E$  relative to that of the  $P4/mbm$  structure. Dashed arrows between the phases mean that the phase connected to the tail of the arrow has a phonon instability leading to the phase connected to the head of the arrow. When no imaginary mode is found in a structure, the structure is denoted as dynamically stable, while structures with imaginary modes are dynamically unstable. Here, we focus on the distorted phases obtained through the condensation of the  $\Gamma_3^-$ ,  $\Gamma_2^-$ , and  $M_1^+M_4^+(a, b)$  modes, which exhibit significant instabilities, as revealed in Fig. 6(a). A polar  $P4bm$  structure is obtained by the freezing of the polar distortion transforming like the irrep  $\Gamma_3^-$  and the subsequent optimization of atomic coordinates and lattice constants. This structural relaxation results in a total-energy reduction of  $-2.0$  meV/atom with respect to the reference  $P4/mbm$  phase. The calculated electric polarization is  $28.5 \mu\text{C}/\text{cm}^2$  for the structure. The  $P4bm$  phase still has imaginary-frequency phonon modes, one of

which leads to the  $Ima2$  phase with further energy reduction ( $\Delta E = -5.8$  meV/atom). The  $Ima2$  symmetry is achieved by a direct sum of irreps  $\Gamma_3^-$  and  $A_5^-(a, a)$ , the latter of which corresponds to the  $\text{NbO}_6$  octahedral tilting mode illustrated in Fig. 6(e). It should be noted that no stable structure is obtained by the  $A_5^-(a, a)$  distortion alone. This implies that the polar  $\Gamma_3^-$  distortion induces the  $A_5^-(a, a)$  instability. The  $Ima2$  phase is dynamically stable. The electric polarization of this phase is  $37.9 \mu\text{C}/\text{cm}^2$ , indicating the enhancement of polarization by the octahedral tilting. Actually, the  $P4bm$  and  $Ima2$  structures are well-known FE phases of TTb compounds [20].

The antipolar  $M_1^+M_4^+(a, b)$  distortion [Fig. 6(c)] allows the  $P4/mbm$  structure to transform to the  $Pmmn$  phase, lowering the total energy by  $-1.6$  meV/atom. The  $Pmmn$  phase shows a phonon instability into the  $Pnma$  phase, resulting from the  $A_5^-(a, a)$  octahedral tilt. The instability of the  $A_5^-(a, a)$  octahedral tilt is also induced by the  $M_1^+M_4^+(a, b)$  distortion. The  $Pnma$  phase is still dynamically unstable, thereby producing lower-energy phases with  $Pmc2_1$  ( $\Delta E = -5.8$  meV/atom),  $Pna2_1$  ( $\Delta E = -5.3$  meV/atom), and  $P2_12_12_1$  ( $\Delta E = -5.3$  meV/atom) symmetry by  $\Gamma_3^-$  polar distortion,  $Z_2^+$  out-of-phase octahedral rotation [Fig. 6(f)], and  $A_5^+$  octahedral rotation [Fig. 6(g)], respectively. All of them are dynamically stable. The  $Pmc2_1$  phase has significant electric polarization ( $28.3 \mu\text{C}/\text{cm}^2$ ) along the pseudo-fourfold axis due to the  $\Gamma_3^-$  polar distortion as in the  $P4bm$  and  $Ima2$  phases. Also, the total energy of the



$Pmc2_1$  phase is almost the same as that of the  $Ima2$  phase. Interestingly, the  $M_1^+M_4^+$  ( $a, b$ ) antipolar distortion coexists with the  $\Gamma_3^-$  polar distortion, although both distortions encompass the Nb-ion motions along the pseudo-fourfold axis. On the other hand, the  $Pna2_1$  phase contains the  $\Gamma_5^-$  polar distortion [Fig. 6(h)], leading to the emergence of polarization in the direction normal to the pseudo-fourfold axis. But this polar phase is regarded as “nearly antipolar” because of a negligibly small amplitude of the  $\Gamma_5^-$  mode and hence a tiny polarization ( $0.3 \mu\text{C}/\text{cm}^2$ ). The  $P2_12_12_1$  phase is antipolar because of its nonpolar symmetry. Adding the other antipolar mode like an irrep  $\Gamma_2^-$  to the reference structure yields energy lowering of  $\Delta E = -1.7 \text{ meV}/\text{atom}$  and symmetry lowering into  $P4_21m$ . The  $P4_21m$  phase is dynamically unstable, and adding the  $A_5^-(a, a)$  octahedral tilt to it produces an  $I\bar{4}$  phase with  $\Delta E = -2.5 \text{ meV}/\text{atom}$ . The  $I\bar{4}$  phase still has an imaginary phonon mode leading to a  $Pnc2$  phase with  $\Delta E = -5.3 \text{ meV}/\text{atom}$ , which is dynamically stable. The  $Pnc2$  phase includes the  $\Gamma_3^-$  polar distortion. But this phase is also considered as “nearly antipolar” because the amplitude of the  $\Gamma_3^-$  mode is negligibly small ( $0.1 \mu\text{C}/\text{cm}^2$ ).

Based on the COHP and BVS analyses, the driving forces behind the polar and antipolar distortions involving the off-centering Nb-ion motion and octahedral tilting and rotation distortions are figured out, as described in the Supplemental Material [60]. The polar  $\Gamma_3^-$  and antipolar  $M_1^+M_4^+$  ( $a, b$ ) distortions are driven by so-called second-order Jahn-Teller (SOJT) effects of Nb ions with the  $d^0$  electronic configuration. The  $A_5^-(a, a)$  octahedral tilting and  $A_5^+(a, a)$  rotation distortions are caused by the need to alleviate underbonding of K and La ions as well as the SOJT effect of Nb ions.

To the best of our knowledge, none of the structures discovered by this stable structure search other than  $P4bm$  and  $Ima2$  have thus far been reported as metastable phases. The dynamically stable polar phases including the  $\Gamma_3^-$  polar distortion, the  $Ima2$  and  $Pmc2_1$  phases, have the total energies of  $\Delta E = -5.8 \text{ meV}/\text{atom}$ , which are marginally lower than those of the dynamically stable antipolar phases including either of the antipolar  $\Gamma_2^-$  or  $M_1^+M_4^+$  ( $a, b$ ) modes, the  $Pna2_1$ ,  $P2_12_12_1$ , and  $Pnc2$  phases ( $\Delta E = -5.3 \text{ meV}/\text{atom}$ ). Thus, our first-principles calculations predict that the total energies of the polar and antipolar phases are comparable to each other, possibly leading to a fascinating dielectric response along the pseudo-fourfold axis, complex phase transitions, and structural defects such as antiphase boundaries regarding the off-centering displacements of Nb ions and  $\text{NbO}_6$  octahedral tilts and rotations. There is a total of five different dynamically stable structures in Fig. 7. To check the dependence on the ionic radius of  $R$ , Fig. 8 plots the total energies of these five structures for  $\text{K}_2\text{RNb}_5\text{O}_{15}$  with  $R = \text{Dy}$ ,  $\text{Gd}$ ,  $\text{Sm}$ ,  $\text{Nd}$ , and  $\text{La}$  with respect to the reference  $P4/mbm$  structure. For all the phases, the total energies monotonously decrease as the  $R$  ionic radius decreases; the energy gain by the distortion relevant to each phase increases with decreasing the ionic radius. Thus, our calculations predict that the phase transition temperatures, where the polar and antipolar distorted structures are destabilized against thermal fluctuation, increase with decreasing the  $R$  ionic radius. This is consistent with the experimental finding that  $T_{C1}$  and  $T_{C2}$  increase as the (average)  $R$  ionic radius decreases [see Fig. 4(a)]. Also,

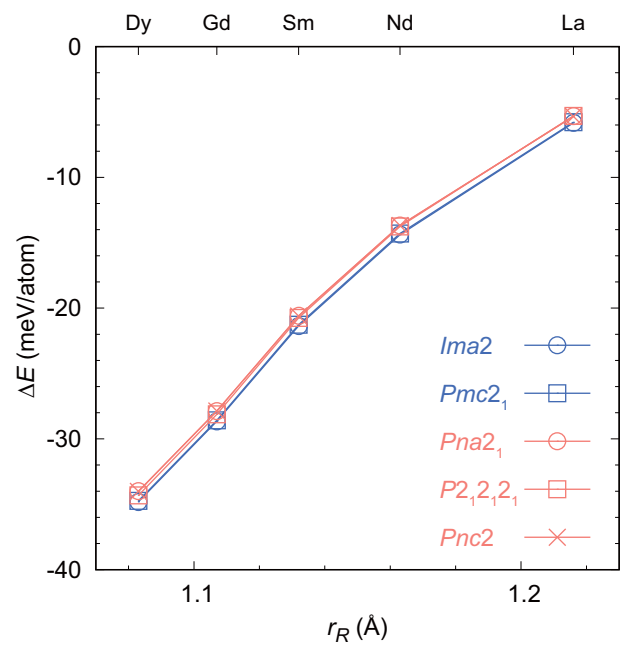


FIG. 8. Total energies of the dynamically stable phases against that of the aristotype  $P4/mbm$  cell as a function of the ionic radius of  $R$  in  $\text{K}_2\text{RNb}_5\text{O}_{15}$ . Polar and antipolar phases are indicated by blue and red colors, respectively, although some of the nearly antipolar phases belong to polar space groups but with negligible electric polarization (see the text).

it should be noted that the total-energy differences between the polar and antipolar phases do not strongly depend on the  $R$  ionic radius, indicating that the coexistence of polar and antipolar instability is a common feature to all the  $\text{K}_2\text{RNb}_5\text{O}_{15}$  compounds.

Our first-principles calculations shed light on the origin of the emerging relaxor behavior that has been experimentally revealed for  $\text{K}_2\text{LaNb}_5\text{O}_{15}$  at below 200 K. The noncollective nature of the off-centering Nb-ion displacements along the pseudo-fourfold axis is reflected by the flat phonon bands with imaginary frequencies along the  $\Gamma$ - $X$ - $M$ - $\Gamma$  line in the  $P4/mbm$  phase of  $\text{K}_2\text{LaNb}_5\text{O}_{15}$ ; there could be a variety of disordered patterns of Nb-ion displacements that stabilize the system at finite temperatures, with the aid of the contribution of entropy to free energy. As revealed by our calculations, the tilts and rotations of the  $\text{NbO}_6$  octahedra are accompanied by off-centering Nb-ion motions. The disordered Nb-ion displacements could yield frustration in the octahedral rotations and tilts, in which neighboring  $\text{NbO}_6$  octahedra are interlocked with each other. The randomness and frustration could disturb the evolution of the FE domain, leading to the observed relaxor behavior. The mechanism of the AFE behavior observed for the smaller rare-earth TTB is also supported by our calculations, which predict the existence of polar and antipolar stable phases with comparable total energies. The emerging antipolar phases are realized in actual systems at finite temperatures, and comparably stable polar phases are induced by applying electric fields.

It must be noted that the antipolar modes obtained in our calculations are inconsistent with a previously assigned space

group for the AFE phase [27]. The authors of Ref. [27] simply assumed space group  $P4nc$  with  $c$  doubling of the aristotype unit cell ( $1 \times 1 \times 2$  expansion) and conducted a Rietveld refinement on laboratory XRD results. As described before, it requires selected area electron diffraction combined with synchrotron x-ray diffraction or powder neutron diffraction to determine exact crystallographic phases for TTB compounds. There is still a lack of direct evidence for space group assignment and internal atomic coordinates. Here, we propose the two candidate antipolar modes without  $c$  doubling,  $\Gamma_2^-$  and  $M_1^+M_4^+$  ( $a, b$ ), based on our stable structure search within  $\sqrt{2} \times \sqrt{2} \times 2$  expansion of the unit cell. Further experimental research is required to determine the exact crystallographic structures of the FE and AFE phases. It may also be necessary to search for stable structures by expanding a unit cell metric, because the calculated phonon bands reveal strong instability at special points such as the  $X$  point.

#### IV. CONCLUSIONS

Antiferroelectricity and its robust dielectric response under high electric fields are experimentally demonstrated in TTB  $K_2RNb_5O_{15}$ . The electrical resistivity and density of ceramics samples were sufficiently improved by optimizing chemical composition and processes, and this enabled us to measure dielectric properties up to high electric field. The typical features of AFE, i.e., a double-hysteresis  $P$ - $E$  loop and a dielectric peak under a DC electric field, were demonstrated at room temperature in  $K_2Pr_{0.75}La_{0.25}Nb_5O_{15}$ , while

the AFE nature disappears and the relaxor nature emerges in  $K_2LaNb_5O_{15}$ . The temperature range of the AFE phase characterized by phase transition temperatures  $T_{C1}$  and  $T_{C2}$  is widely controllable by changing the ionic radius of  $R$  at the A1 sites. Significantly robust relative permittivity against DC field, which might be applicable to MLCCs for high-voltage usage, is realized owing to AFE. The dielectric constant under a high DC electric field of  $K_2Pr_{0.75}La_{0.25}Nb_5O_{15}$ ,  $\sim 800$  at 10 MV/m, exceeds that of  $BaTiO_3$ ,  $\sim 620$  at 10 MV/m. First-principles calculations revealed competing polar and antipolar instabilities, which is a common feature to all the  $K_2RNb_5O_{15}$  compounds, underlying the relaxor behavior and the successive phase transitions of FE-AFE-PE. Two different types of antipolar displacement patterns ( $\Gamma_2^-$  and  $M_1^+M_4^+$ ) were found and are considered to be the structural origin of the AFE nature in TTB, though further research is required to determine the exact crystallographic structure. We hope that this research encourages and inspires more research activities to design new AFEs in other crystallographic systems than conventional perovskites.

#### ACKNOWLEDGMENTS

We are grateful to Toru Asaka, Finlay Morrison, and James F. Scott for many fruitful discussions. We would like to thank Sayoko Aoki for her assistance in our experiments and Y. Inoue and K. Honda for preparing Pt paste. The computation was carried out using the computer resource offered under the category of General Projects by Research Institute for Information Technology, Kyushu University.

- 
- [1] H. Kishi, Y. Mizuno, and H. Chazono, *Jpn. J. Appl. Phys.* **42**, 1 (2003).
  - [2] C. Kittel, *Phys. Rev.* **82**, 729 (1951).
  - [3] X. Tan, C. Ma, J. Frederick, S. Beckman, and K. G. Webber, *J. Am. Ceram. Soc.* **94**, 4091 (2011).
  - [4] A. Chauhan, S. Patel, R. Vaish, and C. R. Bowen, *Materials (Basel)* **8**, 8009 (2015).
  - [5] S. E. Young, J. Y. Zhang, W. Hong, and X. Tan, *J. Appl. Phys.* **113**, 054101 (2013).
  - [6] H. Zhang, X. Chen, F. Cao, G. Wang, X. Dong, Z. Hu, and T. Du, *J. Am. Ceram. Soc.* **93**, 4015 (2010).
  - [7] G. Shirane, E. Sawaguchi, and Y. Takagi, *Phys. Rev.* **84**, 476 (1951).
  - [8] L. E. Cross, *J. Phys. Soc. Jpn.* **23**, 77 (1967).
  - [9] X. Hao and J. Zhai, *J. Phys. D: Appl. Phys.* **40**, 7447 (2007).
  - [10] W. Pan, Q. Zhang, A. Bhalla, and L. E. Cross, *J. Am. Ceram. Soc.* **72**, 571 (1989).
  - [11] D. Berlincourt, H. H. A. Krueger, and B. Jaffe, *J. Phys. Chem. Solids* **25**, 659 (1964).
  - [12] E. Sawaguchi, H. Maniwa, and S. Hoshino, *Phys. Rev.* **83**, 1078 (1951).
  - [13] G. Shirane, R. Newnham, and R. Pepinsky, *Phys. Rev.* **96**, 581 (1954).
  - [14] H. Shimizu, H. Guo, S. E. Reyes-Lillo, Y. Mizuno, K. M. Rabe, and C. A. Randall, *Dalton Trans.* **44**, 10763 (2015).
  - [15] Y. B. Yao, C. L. Mak, and B. Ploss, *J. Eur. Ceram. Soc.* **32**, 4353 (2012).
  - [16] J. Gardner and F. D. Morrison, *Dalton Trans.* **43**, 11687 (2014).
  - [17] J. Gardner and F. D. Morrison, *Appl. Phys. Lett.* **109**, 072901 (2016).
  - [18] S. C. Abrahams, P. B. Jamieson, and J. L. Bernstein, *J. Chem. Phys.* **54**, 2355 (1971).
  - [19] X. Zhu, M. Fu, M. C. Stennett, P. M. Vilarinho, I. Levin, C. A. Randall, J. Gardner, F. D. Morrison, and I. M. Reaney, *Chem. Mater.* **27**, 3250 (2015).
  - [20] M. Smirnov and P. Saint-Grégoire, *Acta Crystallogr., Sect. A: Found. Adv.* **70**, 283 (2014).
  - [21] P. Labbe, H. Leligny, B. Raveau, J. Schneck, and J. C. Toledano, *J. Phys.: Condens. Matter* **2**, 25 (1990).
  - [22] I. Levin, M. C. Stennett, G. C. Miles, D. I. Woodward, A. R. West, and I. M. Reaney, *Appl. Phys. Lett.* **89**, 122908 (2006).
  - [23] M. H. Francombe and B. Lewis, *Acta Crystallogr.* **11**, 696 (1958).
  - [24] Y. Amira, Y. Gagou, A. Menny, D. Mezzane, A. Zegzouti, M. Elaatmani, and M. El Marssi, *Solid State Commun.* **150**, 419 (2010).
  - [25] B. A. Scott, E. A. Giess, G. Burns, and D. F. O'Kane, *Mater. Res. Bull.* **3**, 831 (1968).
  - [26] R. R. Neurgaonkar, J. G. Nelson, J. R. Oliver, and L. E. Cross, *Mater. Res. Bull.* **25**, 959 (1990).
  - [27] Y. Gagou, Y. Amira, I. Lukyanchuk, D. Mezzane, M. Courty, C. Masquelier, Y. I. Yuzuk, and M. El Marssi, *J. Appl. Phys.* **115**, 064104 (2014).

- [28] P. E. Blöchl, *Phys. Rev. B* **50**, 17953 (1994).
- [29] G. Kresse and D. Joubert, *Phys. Rev. B* **59**, 1758 (1999).
- [30] J. P. Perdew, K. Burke, and M. Ernzerhof, *Phys. Rev. Lett.* **78**, 1396 (1997).
- [31] J. P. Perdew, K. Burke, and M. Ernzerhof, *Phys. Rev. Lett.* **77**, 3865 (1996).
- [32] J. P. Perdew, A. Ruzsinszky, G. I. Csonka, O. A. Vydrov, G. E. Scuseria, L. A. Constantin, X. Zhou, and K. Burke, *Phys. Rev. Lett.* **100**, 136406 (2008).
- [33] G. Kresse and J. Furthmüller, *Comput. Mater. Sci.* **6**, 15 (1996).
- [34] G. Kresse and J. Hafner, *Phys. Rev. B* **47**, 558 (1993).
- [35] G. Kresse and J. Hafner, *Phys. Rev. B* **48**, 13115 (1993).
- [36] G. Kresse and J. Furthmüller, *Phys. Rev. B* **54**, 11169 (1996).
- [37] A. Togo, F. Oba, and I. Tanaka, *Phys. Rev. B* **78**, 134106 (2008).
- [38] H. J. Monkhorst and J. D. Pack, *Phys. Rev. B* **13**, 5188 (1976).
- [39] A. Ganose, A. Jackson, and D. Scanlon, *J. Open Source Softw.* **3**, 717 (2018).
- [40] A. Togo and I. Tanaka, [arXiv:1808.01590v1](https://arxiv.org/abs/1808.01590v1).
- [41] H. T. Stokes, D. M. Hatch, B. J. Campbell, and D. E. Tanner, *J. Appl. Crystallogr.* **39**, 607 (2006).
- [42] S. Maintz, V. L. Deringer, A. L. Tchougréeff, and R. Dronskowski, *J. Comput. Chem.* **37**, 1030 (2016).
- [43] S. Maintz, V. L. Deringer, A. L. Tchougréeff, and R. Dronskowski, *J. Comput. Chem.* **34**, 2557 (2013).
- [44] R. Dronskowski and P. E. Bloechl, *J. Phys. Chem.* **97**, 8617 (1993).
- [45] V. L. Deringer, A. L. Tchougréeff, and R. Dronskowski, *J. Phys. Chem. A* **115**, 5461 (2011).
- [46] M. O'Keefe and N. E. Brese, *J. Am. Chem. Soc.* **113**, 3226 (1991).
- [47] S. P. Ong, W. D. Richards, A. Jain, G. Hautier, M. Kocher, S. Cholia, D. Gunter, V. L. Chevrier, K. A. Persson, and G. Ceder, *Comput. Mater. Sci.* **68**, 314 (2013).
- [48] K. Momma and F. Izumi, *J. Appl. Crystallogr.* **44**, 1272 (2011).
- [49] J. Gardner, F. Yu, C. Tang, W. Kockelmann, W. Zhou, and F. D. Morrison, *Chem. Mater.* **28**, 4616 (2016).
- [50] L. E. Cross, *Ferroelectrics* **76**, 241 (1987).
- [51] R. D. Shannon, *Acta Crystallogr., Sect. A: Found. Adv.* **32**, 751 (1976).
- [52] M. C. Stennett, I. M. Reaney, G. C. Miles, D. I. Woodward, A. R. West, C. A. Kirk, and I. Levin, *J. Appl. Phys.* **101**, 104114 (2007).
- [53] X. L. Zhu, X. Q. Liu, and X. M. Chen, *J. Am. Ceram. Soc.* **94**, 1829 (2011).
- [54] K. Li, X. L. Zhu, X. Q. Liu, X. Ma, M. Sen Fu, J. Kroupa, S. Kamba, and X. M. Chen, *NPG Asia Mater.* **10**, 71 (2018).
- [55] O. E. Fesenko, R. V. Kolesova, and Y. G. Sindeyev, *Ferroelectrics* **20**, 177 (1978).
- [56] G. H. Olsen, U. Aschauer, N. A. Spaldin, S. M. Selbach, and T. Grande, *Phys. Rev. B* **93**, 180101(R) (2016).
- [57] G. H. Olsen, M. H. Sørby, S. M. Selbach, and T. Grande, *Chem. Mater.* **29**, 6414 (2017).
- [58] S. S. Aamlid, S. M. Selbach, and T. Grande, *Materials (Basel)* **12**, 1156 (2019).
- [59] H. Djani, E. E. McCabe, W. Zhang, P. S. Halasyamani, A. Feteira, J. Bieder, E. Bousquet, and P. Ghosez, *Phys. Rev. B* **101**, 134113 (2020).
- [60] See Supplemental Material at <http://link.aps.org/supplemental/10.1103/PhysRevMaterials.4.104419> for information on the analyses of electronic structures and crystallochemical parameters.